JPhys Energy

PAPER • OPEN ACCESS

Barocaloric response of plastic crystal 2-methyl-2-nitro-1-propanol across and far from the solid-solid phase transition

Journal of Physics: Energy

OPEN ACCESS

RECEIVED
15 May 2023

REVISED
23 September 2023

ACCEPTED FOR PUBLICATION
12 October 2023

PUBLISHED
25 October 2023

PAPER

Barocaloric response of plastic crystal 2-methyl-2-nitro-1-propanol across and far from the solid-solid phase transition

Alejandro Salvatori[1,2], **María Barrio**[1,2], **Philippe Negrier**[3], **Stéphane Massip**[4], **Michela Romanini**[1,2], **Araceli Aznar**[1,2], **Pol Lloveras**[1,2,*] and **Josep-Lluís Tamarit**[1,2]

[1] Grup de Caracterització de Materials, Departament de Física, EEBE, Campus Diagonal-Besòs, Universitat Politècnica de Catalunya, Eduard Maristany, 10-14, 08019 Barcelona, Catalonia, Spain
[2] Barcelona Research Center in Multiscale Science and Engineering, Universitat Politècnica de Catalunya, Eduard Maristany, 10-14, 08019 Barcelona, Catalonia, Spain
[3] Université de Bordeaux, LOMA, UMR 5798, F33400 Talence, France
[4] Université de Bordeaux, CNRS, INSERM, IECB, UAR 3033, F-33600 Pessac, France
[*] Author to whom any correspondence should be addressed.

E-mail: pol.lloveras@upc.edu

Keywords: barocaloric, plastic crystal, entropy, phase transition, calorimetry, diffraction

Abstract

Plastic crystals have emerged as benchmark barocaloric (BC) materials for potential solid-state cooling and heating applications due to huge isothermal entropy changes and adiabatic temperature changes driven by pressure. In this work we investigate the BC response of the neopentane derivative 2-methyl-2-nitro-1-propanol ($NO_2C(CH_3)_2CH_2OH$) in a wide temperature range using x-ray diffraction, dilatometry and pressure-dependent differential thermal analysis. Near the ordered-to-plastic transition, we find colossal BC effects of $\simeq$400 J K^{-1} kg^{-1} and $\simeq$5 K upon pressure changes of 100 MPa. Although reversible effects at the transition are obtained only from higher pressure changes due to hysteretic effects, we do obtain fully reversible BC effects from any pressure change in individual phases, that become giant at moderate pressures due to very large thermal expansion, especially in the plastic phase. From our measurements, we also determine the crystal structure of the low-temperature phase and estimate the contribution of the configurational disorder and the volume change to the total transition entropy change.

1. Introduction

Plastic crystals feature phase transitions with a very large latent heat among solid–solid phase transitions, which are typically associated with the emergence of orientational disorder in the plastic phase [1]. While these *phase change materials* have traditionally attracted interest for passive thermal energy management [2], recent studies have reported in these materials unrivaled isothermal entropy changes and large adiabatic temperature changes driven by pressure changes thanks to the significant sensitivity of the phase transition to pressure. These barocaloric (BC) effects could be functionalized in more sustainable coolers and heat pumps [3–5], as a potential solution to the environmental thread posed by billions of current appliances that use potent greenhouse hydrofluorocarbon fluids. Similarly, BC effects in plastic crystals have also been proposed for thermal energy management actively controlled by pressure [6, 7]. Furthermore, plastic crystals are, overall, of null or low toxicity, cheap and readily available. In addition, as any other BC material, their use in form of powder makes the drawback of fatigue disappear.

Based on phase transition equilibrium properties at atmospheric pressure available in the literature [1], molecular plastic crystals can be preselected as potentially among the best BC materials. However, some of them are actually limited or not suited for BC cooling and heating due to irreversibility issues and a deeper analysis including high-pressure and out-of-equilibrium data is needed to determine the actual BC performance of any compound. To date, the BC performance of different molecular plastic crystal families has been investigated: organic compounds as neopentane derivatives [3–5, 8] and adamantane derivatives [6,

9], and inorganic compounds as carboranes [10]. Neopentane derivatives have shown by far the largest BC effects, but some of the adamantane derivatives and carboranes exhibit a better reversible BC performance at lower pressures due to relatively low transition hysteresis. Here it must be pointed out that many plastic crystals, and in particular neopentane derivatives, typically show a very large volumetric thermal expansion $\alpha \sim 10^{-4}\,\mathrm{K}^{-1}$ in individual phases [11], which exceeds one order of magnitude or more the typical values achieved by other BC materials, and that is comparable with that of polymers [12] and spin-crossover compounds [13]. This anticipates significant BC effects also in individual phases which, interestingly, are fully reversible upon any pressure change because they do not involve hysteresis associated with first-order phase transitions. However, this contribution has often been overlooked, thus underrating the overall BC response of these materials. In this work we investigate the BC response of the neopentane derivative 2-methyl-2-nitro-1-propanol (MNP, with chemical formula $NO_2C(CH_3)_2CH_2OH$) both across the ordered-to-plastic phase transition and in each individual phase. For this purpose we use single crystal and powder x-ray diffraction, high-pressure dilatometry, modulated calorimetry and differential thermal analysis at high pressures.

2. Experimental

MNP ($NO_2C(CH_3)_2CH_2OH$) was purchased in powder form from Sigma-Aldrich with a purity of 99% and used as received. A single crystal of MNP in the ordered phase was obtained by sublimation.

Crystallographic data of MNP samples were collected at 153 K with a R-Axis Rapid Rigaku MSC diffractometer with monochromatic Cu-Kα radiation ($\lambda = 1.541\,87$ Å) and a curved image plate detector. The unit cell determination and data reduction were performed using the Crystal Clear program suite [14] on the full set of data. The structure was solved by direct methods and refined using Shelx 97 suite of programs [15] in the integrated WinGX system [16]. The H coordinates of the hydroxyl group were refined. The positions of all the other H atoms were deduced from coordinates of the non-H atoms and confirmed by Fourier synthesis [17]. These H atoms were included for structure factor calculations but not refined, as usual. The non-H atoms were refined with anisotropic temperature parameters.

High-resolution x-ray powder diffraction (XRPD) was performed at atmospheric pressure and as a function of temperature using Cu-K$\alpha_1 = 1.540\,56$ Å radiation in an INEL diffractometer with a curved-quartz monochromator, a cylindrical position-sensitive detector (CPS-120) and the Debye-Scherrer geometry. Powder MNP was introduced into a 0.5 mm diameter Lindemann capillary, and a 600 series Oxford Cryostream Cooler was used to control temperature. The Materials Studio software [18] was used to determine the lattice parameters for the high-temperature cubic (C) and low-temperature monoclinic (M) phases by the Pawley method and the crystal structure at 100 K by Rietveld refinement, respectively.

High-pressure dilatometry measurements were performed using custom-built *pVT* apparatus (uncertainty of ca. $10^{-4}\,\mathrm{g\,cm}^{-3}$) from the high-pressure laboratory of Prof. Dr A Würflinger (Ruhr-Universität, Bochum, Germany). Around 2 g of MNP were sealed in liquid form to remove air bubbles, in stainless-steel cells. Relative volume changes caused the movement of a Bridgman piston placed inside a coil, which could be determined due to electromagnetic induction [19]. Absolute volume was calculated using data obtained from x-ray diffraction at normal pressure. Further details of the experimental system and the procedure have been reported elsewhere [20].

Differential scanning calorimetry at atmospheric pressure was carried out using a DSC Q100 and DSC250 (TA Instruments), with ∼5 mg of powder MNP encapsulated in aluminum pans. Temperature ramps were performed at 2–10 K min^{-1}. Heat capacity experiments were performed in a DSC250 (TA Instruments) by means of modulated calorimetry with a modulation period of 120 s, a modulation amplitude of 2 K and a temperature rate of 2 K min^{-1}.

High-pressure differential thermal analysis (HP-DTA) was performed using two bespoke Cu-Be high-pressure calorimeters. One can achieve pressures up to ∼0.3 GPa and operates with Bridgman pistons with K-type thermocouples and the other is a MV1-30 pressure cell (Unipress, Poland) that can achieve pressures up to ∼0.6 GPa and uses Peltier modules as thermal sensors. In both calorimeters, temperature is controlled by means of an external thermal jacket connected to a Lauda Proline RP 1920 refrigerating circulator, within a temperature range from 205 K to 393 K. Temperature rates were ∼2 K min^{-1}. A few hundreds of mg of MNP were sealed in Sn capsules in liquid form to remove air. The pressure-transmitting fluid was DW-Therm M90.200.02 (Huber).

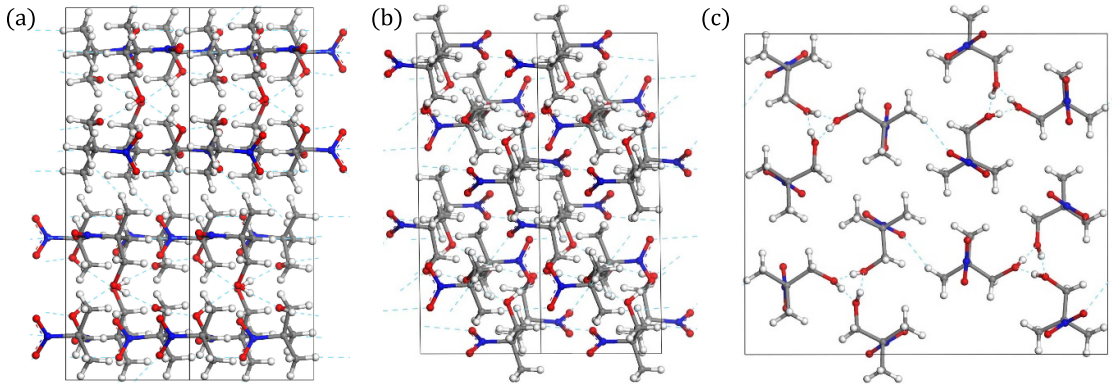

Figure 1. Crystal structure of the unit cell of the monoclinic phase for MNP (a) along *c*, (b) along *b* and (c) along *a* crystallographic axes. Blue, red, grey and white atoms stand for N, O, C and H. Cyan dashed lines stand for hydrogen bonds.

Table 1. Overlay of molecules identified by their hydroxyl label.

Molecules overlay	RMSD (Å)	Dev max (Å)
O1/O11	0.0117	0.0199
O1/O21	0.047	0.0937
O11/O21	0.0384	0.0768

Table 2. H bonds with distances and angle details. O1, O11, O21 belong to hydroxyl groups whereas O6, O15 and O25 belong to nitro groups.

D	H	A	d(H···A) (Å)	d(D···A) (Å)	(D-H···A) deg.	symm(A)
O1	H1	O11	1.81(2)	2.625(2)	173(3)	.
O11	H11	O21	1.79(3)	2.628(2)	171(2)	2_745
O21	H21	O1	1.80(3)	2.623(2)	172(3)	2_655
C7	H7A	O1	2.59	2.934(2)	101	.
C7	H7C	O6	2.58	3.555(2)	174	1_655
C8	H8C	O25	2.54	3.461(3)	156	1_445
C18	H18A	O11	2.59	2.941(2)	101	.
C18	H18C	O15	2.58	3.556(2)	173	1_655

3. Results and discussion

Chemically, neopentane molecule $C(CH_3)_4$ consists of a carbon linked to four methyl groups and displays achiral tetrahedral symmetry [21] and its derivatives are obtained by substitution of some of the methyl groups. Physically, neopentane and its derivatives undergo an endothermic first-order phase transition from an ordered phase to a cubic plastic phase, whose transition properties such as temperature, latent heat and volume change depend significantly on each particular derivative [22]. MNP is a neopentane derivative obtained by the substitution of two methyl groups by one nitro group and one hydroxyl group. At room temperature and at atmospheric pressure, MNP molecules arrange in a monoclinic symmetry [23] (phase M for short, space group $P2_1/c$, $Z = 12$). Upon heating, at 310 K MNP transforms to a face centered cubic (fcc, C for short) phase through a first-order phase transition with a very large enthalpy change determined to be within the range $\simeq$15.0–17.2 kJ mol^{-1} [11, 24–26]. This is much higher than the enthalpy change at the melting at 364 K (3.4–3.7 kJ mol^{-1}), as typically occurs in plastic crystals.

3.1. Structural and thermodynamic characterization

The crystal structure of the M phase (see figure 1) was determined from single crystal x-ray diffraction at 153 K (cif number: CCDC 2253858, see figure 2(a)). The asymmetric unit contains three independent molecules that differ little from each other (see table 1). The crystalline cohesion is ensured by the two types of hydrogen bonds (see table 2). The first type corresponds to hydrogen bonds of type O–H···O between the hydroxyl groups of the three independent molecules. They are organized in helices in a single direction, parallel to the *Ox* crystallographic axis, with coordinates close to $x; 1/4; 1/4$ and their symmetrical. The other

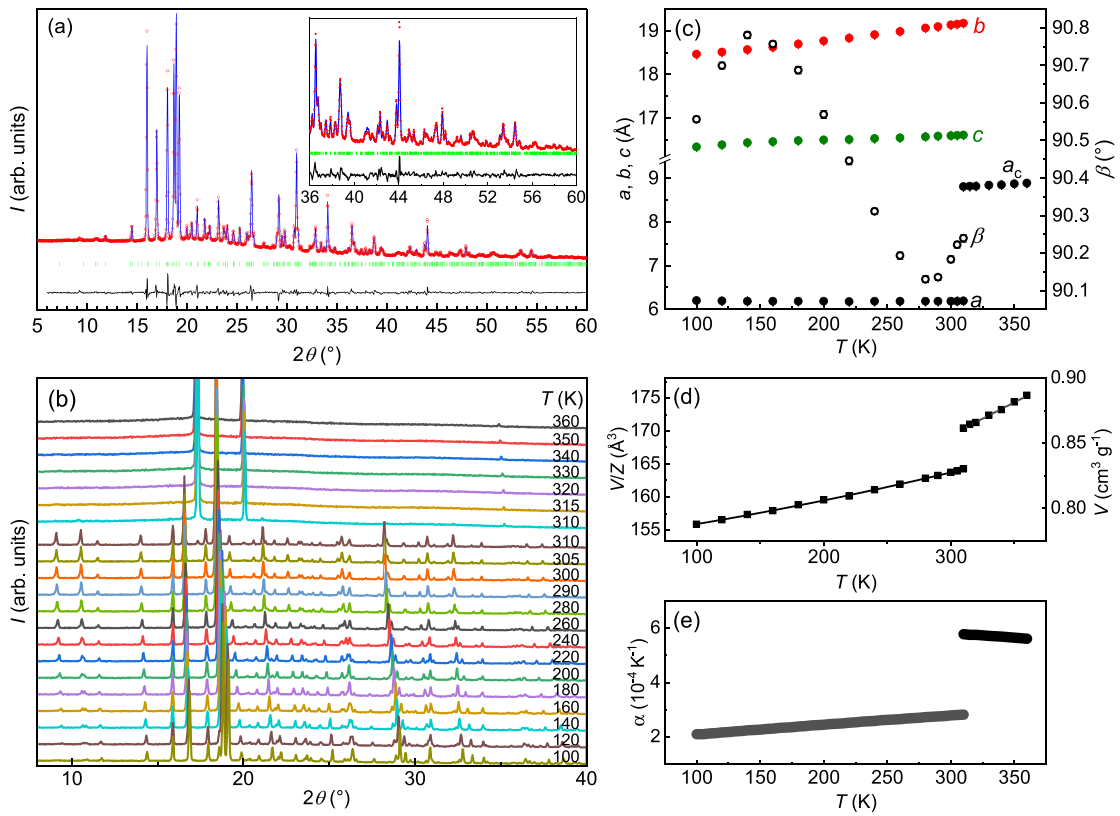

Figure 2. XRPD measurements. (a) Refined powder diffraction pattern in the monoclinic phase at 100 K. The inset shows a high-angle interval enlarged 6 times. Red symbols are experimental data, blue lines are refined profiles, green segments indicate Bragg peak positions and black lines are differences between calculated and experimental data. (b) XRPD patterns at different temperatures across the phase transition. (c) Lattice parameters as a function of temperature. Monoclinic parameters are a, b, c (left axis) and β (right axis) and the cubic parameter is a_c (left axis). (d) Temperature-dependent volume per formula unit (left axis) and per unit of mass (right axis). (e) Thermal expansion as a function of temperature.

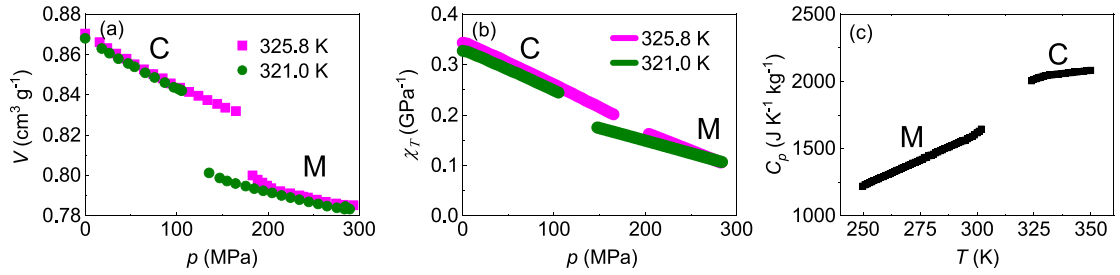

Figure 3. (a) Volume and (b) isothermal compressibility as a function of pressure at two different temperatures. (c) Heat capacity at atmospheric pressure as a function of temperature.

hydrogen bonds are of type O···H–C and ensure the crystalline cohesion in directions parallel or orthogonal to the first. The strength of the O–H···O type H-bonds can be emphasized through their donor-acceptor distance (only 285 hits in the CSD in the distance range 2.63 (2) Å with $R1 < 0.1$ and 149 hits if we also take into account an O–H···O angle $> 165°$).

XRPD performed at different temperatures across the transition (see figure 2(b)) allowed to determine the temperature dependence of lattice parameters (see figure 2(c)), and hence volume (see figure 2(d)). The obtained discontinuity indicates the occurrence of the first-order phase transition with a volume change at the endothermic transition of $\Delta V_t \simeq 0.32 \times 10^{-4}$ m^3 kg^{-1}, which corresponds to a very large relative change of $\frac{\Delta V_t}{V} \simeq 3.8\%$. Using a second-order polynomial and a linear fit for $V(T)$ in phase M and C, respectively, the thermal expansion coefficient α was determined (see figure 2(e)).

Volume was measured isothermally at 321.0 K and 325.8 K on decompression across the phase transition (see figure 3(a)). From the sharp increase in volume associated with the phase transition, two points of the coexistence line $T(p)$ of the phase diagram (see empty triangles in figure 4(b)) and the associated transition

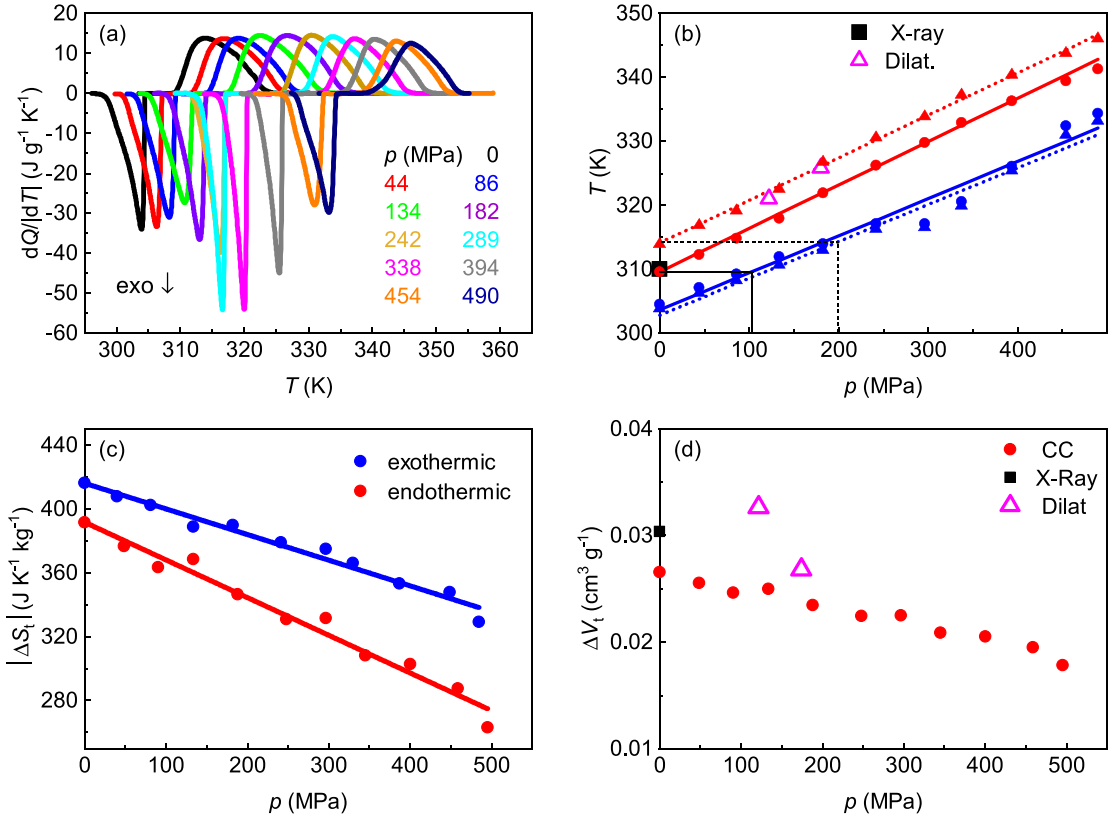

Figure 4. Characterization at high pressure. (a) Isobaric HP-DTA as a function of temperature at different pressures on heating (positive) and on cooling (negative) across the transition. (b) Temperature-pressure phase diagram for the endothermic (red) and for the exothermic transitions (blue). Circles and triangles stand for the onset and maximum of the peaks, respectively. Continuous and dashed lines are fits to peak onsets and maximums. Data from XRPD and dilatometry are also included. (c) Entropy change at endothermic (red) and exothermic (blue) transitions as a function of pressure. (d) Volume change at the endothermic transition obtained via: (i) XRPD at atmospheric pressure as derived from figure 2(d) (square); (ii) dilatometry as derived from figure 3(a) (triangles) and (iii) the Clausius-Clapeyron (CC) equation at different pressures (circles).

volume changes (see empty triangles in figure 4(c)) were determined. By fitting $V(p)$ data in each phase, the isothermal compressibility χ_T was calculated (see figure 3(b)). Heat capacity was measured at atmospheric pressure as a function of temperature (see figure 3(c)), yielding values in agreement with literature values within uncertainty [25].

Heat flow at atmospheric pressure (not shown) yielded an endothermic peak with onset transition temperatures at $\simeq$310 K associated with the latent heat of the equilibrium first-order phase transition. Peak integration after baseline subtraction yielded a latent heat $\Delta H_t \simeq 121\,\mathrm{J\,g^{-1}}$ whereas integration of the peak in $\frac{\dot{Q}}{T}$ after baseline subtraction yielded the transition entropy change $\Delta S_t \simeq 391\,\mathrm{J\,K^{-1}\,kg^{-1}}$, in good agreement with literature values [25, 26]. In this family of materials, this quantity is typically expected to be mainly contributed by changes in the number of configurations (both orientational and conformational) and in the transition volume change. In phase C, MNP has ten possible orientations, each of which has nine different conformations derived from the fact that both nitro and hydroxyl groups have each three different conformations. This yields a total number of configurations of $N_C = 90$ for phase C whereas $N_M = 1$ for the fully ordered phase M, which leads to a configurational entropy change $\Delta S_c = RM^{-1} \ln \frac{N_C}{N_M} = 314\,\mathrm{J\,K^{-1}\,kg^{-1}}$ (R is the universal gas constant and M the molar mass). In turn, the volumetric entropy change can be estimated using [27, 28] $\Delta S_V = \frac{\langle\alpha\rangle}{\langle\chi_T\rangle}\Delta V_t$ where $\langle\alpha\rangle$ and $\langle\chi_T\rangle$ are averaged over the two phases close to the transition. In particular, from figure 2(e) we calculate $\langle\alpha\rangle \simeq 4.3\times10^{-4}\,\mathrm{K^{-1}}$ and from figure 3(b), $\langle\chi_T\rangle \simeq 0.22\ \mathrm{GPa^{-1}}$, which yields $\Delta S_V \simeq 62\,\mathrm{J\,K^{-1}\,kg^{-1}}$. As expected, we obtain $\Delta S_c + \Delta S_V \simeq \Delta S_t$ and confirm that the major contribution to the total entropy change at the transition is due to the emergence of the molecular orientational and conformational disorder.

Heat flow in temperature $\frac{dQ}{d|T|} = \frac{\dot{Q}}{|\dot{T}|}$ recorded by means of HP-DTA at different constant pressures is shown in figure 4(a). Notice that the peaks obtained on cooling are narrower, hence more abrupt, than those on heating, consistently with the out-of-equilibrium nature of hysteretic exothermic transitions. The in- and out-of-equilibrium $T(p)$ phase diagram (see figure 4(b)) was constructed using peak temperatures in HP-DTA (circles for the peak onset, filled triangles for the peak maximum), and, as mentioned previously,

data from x-ray diffraction from figure 2(d) (black square) and dilatometry from figure 3(a) (empty triangles). Values of $\frac{dT}{dp} \simeq 67\,\mathrm{K\,GPa^{-1}}$ and $\frac{dT}{dp} \simeq 58\,\mathrm{K\,GPa^{-1}}$ were obtained for the endothermic and exothermic transitions, respectively. From the phase diagram, the minimum pressure to achieve reversible effects (p_{rev}) can be determined as the pressure at which the exothermic transition temperature equals the endothermic transition temperature at atmospheric pressure. As discussed elsewhere [8] and applied here later on, by using the onset transition temperature we obtain $p_{rev} \simeq 100$ MPa (see continuous black lines) for reversible isothermal entropy changes whereas by using the peak maximum we obtain $p_{rev} \simeq 200$ MPa (see dashed black lines) for reversible adiabatic temperature changes.

Entropy change at the transition as a function of pressure (see figure 4(c)) was found to decrease with pressure at a rate of $\frac{d|\Delta S_t|}{dp} \simeq -0.24\,\mathrm{J\,K^{-1}\,kg^{-1}\,MPa^{-1}}$. The feature $\frac{d|\Delta S_t|}{dp} < 0$ is usually observed in this family of materials and in other organic plastic crystals [3, 6, 8, 9]. Volume change at the transition as a function of pressure (see figure 4(d)) was determined from x-ray diffraction (figure 2(d)), dilatometry (figure 3(a)) and the Clausius–Clapeyron equation $\Delta V_t = \frac{dT}{dp}\Delta S_t$ from figures 4(b) and (c). While overall there is a good agreement between data from different experiments, the point derived from dilatometry at 321.0 K (see green symbols in figure 3(a)) is somewhat out of trend. This can be ascribed to the appearance of pretransitional effects.

3.2. Determination of the BC effects

From our $V(T)$ (figure 2(d)) and heat capacity C_p (figure 3(c)) at atmospheric pressure, and pressure- and temperature-dependent heat flow data associated with the transition $\frac{dQ}{dT}$ (figure 4(a)), we calculated the entropy as a function of temperature and pressure $S(T,p)$ with respect to a reference value at temperature $T_0 = 250$ K and at atmospheric pressure $S(T_0, p_{atm})$ using the following equation:

$$S(T,p) - S(T_0,p_{atm}) = \int_{T_0}^{T} \frac{1}{T}\left(C_p + \frac{dQ}{dT}\right) dT - \int_{p_{atm}}^{p} \left(\frac{\partial V}{\partial T}\right)_{T_0;p} dp. \quad (1)$$

Given that at $T > T_0$, the volume of each phase is nearly linear with temperature (see figure 2(d)), the thermodynamic equation $(\frac{\partial C_p}{\partial p})_T = -T(\frac{\partial^2 V}{\partial T^2})_p$ establishes that C_p is approximately independent of pressure in that regime. On the other hand, to account for the pressure dependence of the transition temperature on C_p, for each phase C_p was extrapolated to high temperatures an incremented range $\frac{dT}{dp}\Delta p$, where $\Delta p = p - p_{atm} \simeq p$. As for the last term in equation (1), we assumed that at T_0 and in the pressure range under analysis, $\left(\frac{\partial V}{\partial T}\right)_{T_0;p}$ is nearly independent of pressure and therefore $\int_{p_{atm}}^{p}\left(\frac{\partial V}{\partial T}\right)_{T_0;p} dp \simeq \left(\frac{\partial V}{\partial T}\right)_{T_0;p_{atm}} \cdot p$, where $\left(\frac{\partial V}{\partial T}\right)_{T_0;p_{atm}} \simeq 2.27 \times 10^{-4}\,\mathrm{cm^3\ g^{-1}\,K^{-1}}$ was calculated at T_0 (i.e. in phase M). This assumption is reasonable given the available data for other compounds of the same family [11] and consistent with the rough trends that can be estimated from $V(p)$ data at two different temperatures in figure 3(a). The resulting entropy functions $S(T,p) - S(T_0,p_{atm})$ are shown in figures 5(a) and (b) for different pressures and as a function of temperature on heating and on cooling, respectively. Interestingly, the isothermal difference of these curves in phase C is consistent within error with the value obtained via $\int_{p_{atm}}^{p}\left(\frac{\partial V}{\partial T}\right)_{T;p} dp \simeq \left(\frac{\partial V}{\partial T}\right)_{T;p_{atm}} \cdot p$, with $\left(\frac{\partial V}{\partial T}\right)_{T;p_{atm}} \simeq 5.0 \times 10^{-4}\,\mathrm{cm^3\ g^{-1}\,K^{-1}}$ calculated in phase C (see the corresponding linear fit in figure 2(d)).

Since MNP exhibits $\frac{dT}{dp} > 0$, isothermal subtraction of entropies obtained on heating and on cooling, independently, yields isothermal entropy changes on first decompression and on first compression, respectively (see figure 5(c)). Adiabatic subtraction of inverted $T(S,p)$ functions, obtained from entropy on heating and on cooling, independently, yields adiabatic temperature changes on first decompression and on first compression, respectively (see figure 5(d)). For cooling and heating applications operating in cycles [29], the need for the refrigerant to transform forth and back in each cycle is hindered by the transition hysteresis. To take into account this feature, the so-called *reversible* BC effects must be determined. Following the standard procedure [8], reversible isothermal entropy changes ΔS_{rev} (see figure 5(e)) are calculated from the overlapping between ΔS on compression and decompression as determined in figure 5(c), and confirm a minimum pressure $p_{rev} \simeq 100$ MPa to obtain non-null ΔS_{rev}. In turn, adiabatic temperature changes ΔT_{rev} (see figure 5(f)) are calculated as differences between the isobaric entropy function on heating at atmospheric pressure and isobaric entropy functions on cooling at pressure p, which confirm a minimum pressure $p_{rev} \simeq 200$ MPa to obtain non-null ΔT_{rev}. As a summary, maximum values for isothermal entropy changes, adiabatic temperature changes and refrigerant capacity RC [30] associated with the first-order phase transition are displayed as a function of pressure in figure 6 for first compressions (blue symbols), first decompressions (red symbols) and reversible processes (green symbols).

A comparison of representative irreversible and reversible values for ΔS and ΔT with other colossal BC materials can be found in table 3. For potential applications related to BC thermal management such as

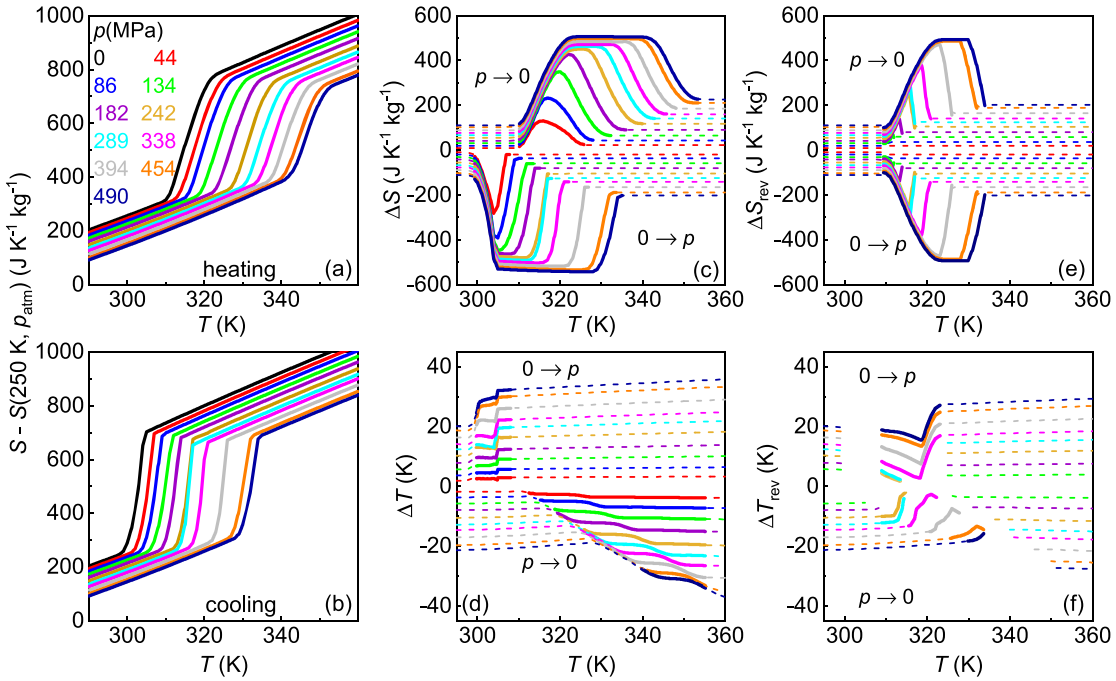

Figure 5. (a) and (b) Entropy $S(T,p)$ with respect to a reference entropy $S(T_0,p_{\rm atm})$ (a) on heating and (b) on cooling. (c) Isothermal entropy changes and (d) adiabatic temperature changes obtained on first compression and on first decompression. Fully reversible (e) isothermal entropy changes and (f) adiabatic temperature changes. In panels (c)–(f), continuous lines correspond to the BC effects involving the first-order phase transition whereas dashed lines correspond to those changes obtained in single phases away from the transition.

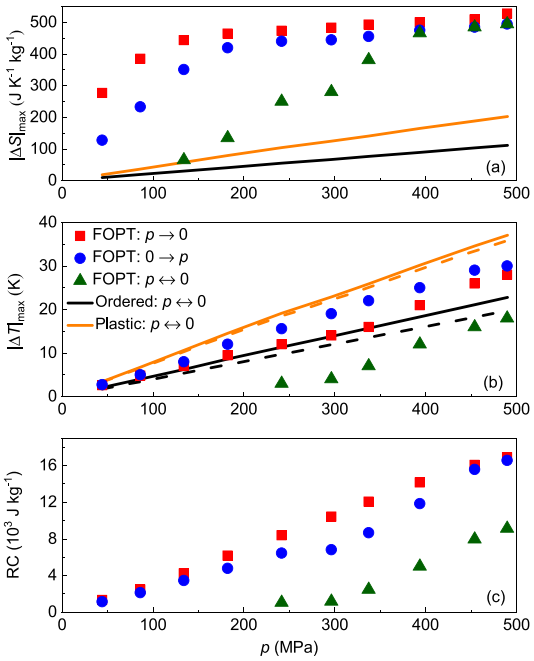

Figure 6. Maximum absolute values of (a) isothermal entropy changes, (b) adabatic temperature changes and (c) Refrigerant Capacity for first compression (blue symbols), first decompression (red symbols) and reversible processes (green symbols) involving the first-order phase transition (FOPT). Orange and black continuous lines refer to (reversible) BC effects obtained away from the transition within the cubic and the monoclinic phases, respectively, from the subtraction of entropy curves. For ΔT, dashed lines are obtained using the equation $|\Delta T| \simeq \frac{T_1}{C_p}|\Delta S|$.

pressure-driven waste heat recovery [6, 7, 31, 32], ΔS is the relevant quantity. Upon a moderate pressure decrease from $\Delta p \simeq 100$ MPa to atmospheric pressure (+86 MPa upon compression), MNP displays $|\Delta S| \simeq 400\,\mathrm{J\,K^{-1}\,kg^{-1}}$, which exceeds most of the values reported previously. For cooling and heating cycles, relevant quantities are $\Delta S_{\rm rev}$ and $\Delta T_{\rm rev}$. In this case the required pressure changes for reversible BC effects

Table 3. Comparison of the irreversible and reversible barocaloric response in plastic crystals and other colossal barocaloric materials. Data for ΔT_{rev} in round brackets are calculated through the approximation $\Delta T_{rev} = |\Delta S_{rev}| T_t / C_p$. Data in curly brackets are obtained from modelling, without taking into account the hysteresis. The acronyms used here have been taken from the corresponding references.

Compound	$\lvert\Delta S\rvert$ J K^{-1} kg^{-1}	p GPa	$\lvert\Delta S_{rev}\rvert$ J K^{-1} kg^{-1}	$\lvert\Delta T_{rev}\rvert$ K	p GPa	References
MNP	400	0.1	150	0	0.2	This work
MNP			450	19	0.5	This work
NPG	370	0.50	421	7.5	0.25	[3]
PG	300	0.40	490	10	0.24	[8]
NPA	250	0.10	293	16	0.26	[8]
TRIS	330	0.50	0	0	0.25	[8]
AMP	600	0.10	0	0	0.25	[8]
1-Br-ada	120	0.50	138	16	0.10	[9]
1-Cl-ada	140	0.20	160	20	0.10	[9]
1-ada-ol	220	0.16	175	11	0.16	[6]
2-ada-ol	100	0.185	100	8	0.185	[6]
2-m-2-ada-ol	360	0.80	300	7	0.08	[6]
C_{60}	30	0.05	26	4	0.05	[33]
Acetoxy Silicone Rubber	160	87	182	21	0.173	[34]
$Li_2B_{12}H_{12}$			{376}	{43}	{0.1}	[35]
$(C_{10}H_2NH_3)_2MnCl_4$	240	0.03	250	10	0.08	[36]
$Fe_3(bntrz)_6(tcnset)_6$	100	0.10	120	35	0.26	[13]
m-carborane	100	0.20	97	(19)	0.05	[10]
NH_4I	70	0.01	71	(34)	0.08	[37]
NH_4SCN	130	0.02				[7]

Table 4. Estimated isothermal entropy changes ΔS_+ upon a pressure change of 0.1 GPa in individual phases for plastic crystals and other colossal BC materials. Here, II and I stand for the ordered or semiordered and disordered phases, respectively.

Material	$\lvert\Delta S_+^{II}\rvert$ (0.1 GPa)	$\lvert\Delta S_+^{I}\rvert$ (0.1 GPa)	References
	J K^{-1} kg^{-1}		
MNP	24	43	This work
NPG	18	38	[3]
PG	60	31	[8]
NPA	39	58	[8]
TRIS	59	45	[8]
AMP	90	20	[8]
1-Br-ada	26.3	57	[9]
1-Cl-ada	18.3	44	[9]
1-ada-ol	16	32	[6]
2-ada-ol	31	44	[6]
2-m-2-ada-ol	19	52	[6]
C_{60}	1.9	3.7	[33]
$(C_{10}H_2NH_3)_2MnCl_4$	$\simeq$0	$\leqslant$10[a]	[36]
$Fe_3(bntrz)_6(tcnset)_6$	14	14	[13]
NH_4I	0.33	0.42	[37]

[a] This value has been estimated from $V(T)$ data.

are larger than for other materials, but still the obtained magnitudes for the BC effects outperform most of other materials.

Despite caloric effects are usually investigated near phase transitions, it may be also interesting to pay special attention to the caloric effects in single phases away from the transition because these are reversible from the first field change as they do not involve hysteretic effects [38] and thus may widen the temperature span useful for applications. In single phases, isothermal entropy changes correspond to those arising due to the last term in equation (1): $\Delta S_{rev} = \Delta S_+ \equiv -\int_{p_0}^{p_1} \left(\frac{\partial V}{\partial T}\right)_p dp$. While these effects are small for many solid materials, plastic crystals in general may display very large isothermal entropy changes due to the large thermal expansion, although they have been typically looked down in previous works. In particular, in MNP, ΔS_{rev} obtained by isothermal subtractions of $S(T,p)$ in single phases (see orange and black lines for phases C and M, respectively in figure 6(a)) are very large, reaching in phase C $|\Delta S_+| \simeq 50$ J K^{-1} kg^{-1} upon pressure changes of $\simeq$180 MPa, and colossal values ($|\Delta S_+| > 100$ J K^{-1} kg^{-1}) for pressure changes $\gtrsim$240 MPa. In table 4 we show a comparison of reversible isothermal entropy changes in individual phases ΔS_+ obtained in

different materials, which reflects that neopentane and adamantane derivatives show indeed very large values. In fact, MNP and NPG exhibit a very similar BC performance, both across and outside the transition, and in similar temperature ranges. Having such a catalog of similar colossal BC materials may be useful because other important features for applications like cost and availability, or methods to tune the transition temperature and hysteresis [39, 40], or thermal conductivity [41, 42] may yield different results in both materials.

In turn, ΔT_{rev} in single phases, which is generally lacking in the literature, has been obtained by two methods: (i) adiabatic subtraction of inverted $T(S,p)$ in single phases (see continuous black and orange lines in figure 6(b) for the M and C phase, respectively) and (ii) calculated via [43] $|\Delta T_{rev}| \simeq \frac{T_t}{C_p}|\Delta S_{rev}|$ (see dashed black and orange lines in figure 6(b) for the M and C phase, respectively). It must be mentioned here that adiabatic temperature changes in single phases are affected by large uncertainties because they may strongly depend on C_p and on the approximation $\left(\frac{\partial V}{\partial T}\right)_p \simeq \left(\frac{\partial V}{\partial T}\right)_{p_{atm}}$ used to estimate the entropy functions $S(T,p)$. Nevertheless, the good agreement between the two methods provides confidence in the obtained ΔT_{rev} which, surprisingly, is larger than those obtained across the first-order phase transition (green symbols in figure 6(b)). More specifically, we obtain $|\Delta T_{rev}| \simeq 8$ K under $\Delta p \simeq 100$ MPa and $|\Delta T_{rev}| \simeq 15$ K under $\Delta p \simeq 200$ MPa.

4. Conclusions

In this work, the BC response of a plastic crystal derived from neopentane, 2-methyl-2-nitro-1-propanol, was investigated via the quasi-direct method using x-ray diffraction, pressure-dependent calorimetry and dilatometry. The structure of the monoclinic phase was determined by single crystal x-ray diffraction and the thermal expansion, the isothermal compressibility and the endothermic and exothermic transition properties were characterized. It was found that the huge transition entropy change emerges mainly due to the orientational and conformational disorder in the plastic phase. As for the BC effects, under a pressure change of 0.1 GPa, we obtained isothermal entropy changes of 400 J K^{-1} kg^{-1} and adiabatic temperature changes of 5 K, thus surpassing most of previously reported plastic crystals and that could be used for potential thermal management applications such as waste heat recovery. Instead, to drive reversibly BC effects associated with the transition that could be used in cooling or heating devices working in cycles, we found a relatively large transition hysteresis that imposes a minimum pressure of ≃0.2 GPa. Therefore, our work confirms that the characterization of the reversible response is key for a proper BC material selection for cooling and heat pumping and that controlling hysteresis is still a major scientific and technological challenge. Notwithstanding, very large and fully reversible BC effects under low pressure changes were found in the individual phases thanks to a large thermal expansion, in particular in the plastic phase. These findings should encourage investigating BC effects also away from phase transitions in this type of materials.

Data availability statement

All data that support the findings of this study are included within the article (and any supplementary files).

Acknowledgments

This work was supported by MINECO Project No. PID2020-112975GB-I00 (Spain) and DGU Project No. 2021SGR-00343 (Catalonia). This work has benefited from the facilities and expertise of the Biophysical and Structural Chemistry plateform (BPCS) at IECB, CNRS UAR3033, Inserm US001, Bordeaux University (www.iecb.u-bordeaux.fr/index.php/en/structural-biophysico-chemistry).

Conflict of interest

Josep-Lluís Tamarit and Pol Lloveras have Patent No. PCT/EP2017/076203 licensed.

ORCID iDs

María Barrio https://orcid.org/0000-0003-3467-7581
Philippe Negrier https://orcid.org/0000-0003-0112-979X
Michela Romanini https://orcid.org/0000-0002-1685-855X
Pol Lloveras https://orcid.org/0000-0003-4133-2223

Josep-Lluís Tamarit https://orcid.org/0000-0002-7965-0000

References

[1] Tamarit J L, Legendre B and Buisine J 1994 *Mol. Cryst. Liq. Cryst. Sci. Technol.* A **250** 347–58
[2] Usman A, Xiong F, Aftab W, Qin M and Zou R 2022 *Adv. Mater.* **34** 2202457
[3] Lloveras P *et al* 2019 *Nat. Commun.* **10** 1803
[4] Li B *et al* 2019 *Nature* **567** 506–10
[5] Lloveras P and Tamarit J L 2021 *MRS Energy Sustain.* **8** 3–15
[6] Salvatori A, Negrier P, Aznar A, Barrio M, Tamarit J L and Lloveras P 2022 *APL Mater.* **10** 111117
[7] Zhang Z *et al* 2023 *Sci. Adv.* **9** eadd0374
[8] Aznar A, Lloveras P, Barrio M, Negrier P, Planes A, Mañosa L, Mathur N D, Moya X and Tamarit J-L 2020 *J. Mater. Chem.* A **8** 639–47
[9] Aznar A, Negrier P, Planes A, Manosa L, Stern-Taulats E, Moya X, Barrio M, Tamarit J-L and Lloveras P 2021 *Appl. Mater. Today* **23** 101023
[10] Zhang K, Song R, Qi J, Zhang Z, Zhang Z, Yu C, Li K, Zhang Z and Li B 2022 *Adv. Funct. Mater.* **32** 2112622
[11] Aznar A, Lloveras P, Barrio M and Tamarit J L 2017 *Eur. Phys. J. Spec. Top.* **226** 1017–29
[12] Usuda E, Bom N M and Carvalho A M G 2017 *Eur. Polym. J.* **92** 287–93
[13] Romanini M *et al* 2021 *Adv. Mater.* **33** 2008076
[14] CrystalClear-SM Expert 2.1 (Rigaku, June 7th 2013), Software, Version 5.6.2.0, Tokyo, Japan
[15] Sheldrick G M 2008 *Acta Crystallogr.* A **64** 112–22
[16] Farrugia L J 1999 *J. Appl. Crystallogr.* **32** 837–8
[17] Spek A L 2015 *Acta Crystallogr.* C **71** 9–18
[18] Ms modeling (Materials Studio), version 5.5 (available at: www.3ds.com/products-services/biovia/products/molecular-modeling-simulation/biovia-materials-studio/) (Accessed 16 october 2023)
[19] Landau R and Würflinger A 1980 *Rev. Sci. Instrum.* **51** 533–5
[20] Würflinger A, Sandmann M and Weissflog W 2000 *Z. Naturforsch.* A **55** 823–7
[21] Mones A H and Post B 1952 *J. Chem. Phys.* **20** 755–6
[22] López D O, Salud J, Tamarit J L, Barrio M and Oonk H A J 2000 *Chem. Mater.* **12** 1108–14
[23] Tamarit J L, Chanh N, Négrier P, López D, Barrio M and Haget Y 1994 *Powder Diffr.* **9** 84–86
[24] Murrill E and Breed L 1970 *Thermochim. Acta* **1** 239–46
[25] Font J and Muntasell J 1994 *Mater. Res. Bull.* **29** 1091–100
[26] Barrio M, López D, Tamarit J L and Haget Y 1995 *Mater. Res. Bull.* **30** 659–69
[27] Sandrock R and Schneider G 1983 *Ber. Bunsenges. Phys. Chem.* **87** 197–201
[28] Jenau M, Reuter J, Tamarit J L and Würflinger A 1996 *J. Chem. Soc. Faraday Trans.* **92** 1899–904
[29] Stern-Taulats E, Planes A, Lloveras P, Barrio M, Tamarit J-L, Pramanick S, Majumdar S, Frontera C and Mañosa L 2014 *Phys. Rev.* B **89** 214105
[30] Gschneidner K Jr and Pecharsky V K 2000 *Annu. Rev. Mater. Sci.* **30** 387–429
[31] Tokoro H *et al* 2015 *Nat. Commun.* **6** 7037
[32] Ohkoshi S-I, Tokoro H, Nakagawa K, Yoshikiyo M, Jia F and Namai A 2019 *Sci. Rep.* **9** 1–8
[33] Li J, Dunstan D, Lou X, Planes A, Mañosa L, Barrio M, Tamarit J-L and Lloveras P 2020 *J. Mater. Chem.* A **8** 20354–62
[34] Imamura W, Usuda E O, Paixão L S, Bom N M, Gomes A M and Carvalho A M G 2020 *Chin. J. Polym. Sci.* **38** 999–1005
[35] Sau K, Ikeshoji T, Takagi S, Orimo S-I, Errandonea D, Chu D and Cazorla C 2021 *Sci. Rep.* **11** 11915
[36] Li J, Barrio M, Dunstan D J, Dixey R, Lou X, Tamarit J-L, Phillips A E and Lloveras P 2021 *Adv. Funct. Mater.* **31** 2105154
[37] Ren Q *et al* 2022 *Nat. Commun.* **13** 2293
[38] Moya X and Mathur N 2020 *Science* **370** 797–803
[39] Barrio M, Font J, Muntasell J, Navarro J and Tamarit J L 1988 *Sol. Energy Mater.* **18** 109–15
[40] Wang C, Li Q, Wang L and Lan X 2016 *Thermochim. Acta* **632** 10–17
[41] Wang X, Guo Q, Zhong Y, Wei X and Liu L 2013 *Renew. Energy* **51** 241–6
[42] Praveen B and Suresh S 2018 *Eng. Sci. Technol. Int. J.* **21** 1086–94
[43] Lloveras P *et al* 2015 *Nat. Commun.* **6** 8801